Atmos. Meas. Tech., 9, 1399–1413, 2016
www.atmos-meas-tech.net/9/1399/2016/
doi:10.5194/amt-9-1399-2016

Atmospheric Measurement Techniques
Open Access
EGU

Observations of water vapor mixing ratio profile and flux in the Tibetan Plateau based on the lidar technique

Songhua Wu[1], **Guangyao Dai**[1], **Xiaoquan Song**[1], **Bingyi Liu**[1], **and Liping Liu**[2]

[1]Ocean Remote Sensing Institute, Ocean University of China, Qingdao, China
[2]Laboratory of Severe Weather, Chinese Academy of Meteorological Science, Beijing, China

Correspondence to: Songhua Wu (wush@ouc.edu.cn)

Received: 7 October 2015 – Published in Atmos. Meas. Tech. Discuss.: 16 November 2015
Revised: 13 March 2016 – Accepted: 22 March 2016 – Published: 1 April 2016

Abstract. As a part of the third Tibetan Plateau Experiment of Atmospheric Sciences (TIPEX III) in China, a Raman water vapor, cloud and aerosol lidar and a coherent wind lidar were operated in Naqu (31.48° N, 92.06° E) with a mean elevation of more than 4500 m a.m.s.l. in summer of 2014. During the field campaign, the water vapor mixing ratio profiles were obtained and validated by radiosonde observations. The mean water vapor mixing ratio in Naqu in July and August was about 9.4 g kg^{-1} and the values vary from 6.0 to 11.7 g kg^{-1} near the ground according to the lidar measurements, from which a diurnal variation of water vapor mixing ratio in the planetary boundary layer was also illustrated in this high-elevation area. Furthermore, using concurrent measurements of vertical wind speed profiles from the coherent wind lidar, we calculated the vertical flux of water vapor that indicates the water vapor transport through updraft and downdraft. The fluxes were for a case at night with large-scale non-turbulent upward transport of moisture. It is the first application, to our knowledge, to operate continuously atmospheric observations by utilizing multi-disciplinary lidars at the altitude higher than 4000 m, which is significant for research on the hydrologic cycle in the atmospheric boundary layer and lower troposphere in the Tibetan Plateau.

1 Introduction

Although the content of water vapor in the atmosphere occupies only about 0.1–3 % of the content of the atmosphere, water vapor has a significant impact on the determination of weather and climate due to the fundamental role in the radiative energy transfer, hydrological cycle and atmospheric chemistry processes. It influences the radiative budget of the planet both directly and through coupling with clouds (Sinha and Harries, 1995; Dinoev et al., 2013). Moreover, because of its strong absorption and emission bands, especially in the infrared, water vapor is the most significant greenhouse gas. Slight changes in the water vapor profile might bring pronounced effect on the global warming process. It also influences atmospheric circulation and temperature structure by condensation and evaporation processes (Peppler and Lamb, 1989; Dinoev, 2009). Aiming at the detection of water vapor, the most commonly used method is radiosonde. The humidity sensors in radiosonde detect changes in resistance or dielectric constant resulting from absorption or adsorption of water (Wang et al., 2003). Several intercomparison studies (Ferrare et al., 1995; Turner and Goldsmith, 1999; Behrendt et al., 2007a, b; Bhawar et al., 2011) have been operated to test the stability of these sensors. As a result, systematic differences between different sensors are present for all ranges of humidity and temperature. Lidar (light detect and ranging), as an active remote sensing technique, has the advantage of high temporal and spatial resolution and high-frequency observations. Two lidar techniques have been applied to the detection of water vapor profile: the Differential Absorption Lidar (DIAL) and the Raman lidar technique. In terms of the DIAL, two laser pulses at different wavelengths, called “online” and “offline” are emitted to the atmosphere (Browell, 1983; Grant, 1991; Wulfmeyer and Bösenberg, 1998; Bruneau et al., 2001; Wirth et al., 2009; Vogelmann and Trickl, 2008). In this paper, the lidar system applies Raman technique. This technique was pioneered by Melfi et al. (1969, 1972) and Cooney (1970) and the profiles of water vapor mixing ratio were retrieved and provided. The

Raman lidar technique depends on the detection of Raman backscattered radiation from atmospheric molecules (Melfi et al., 1969, 1972; Renaut and Capitini, 1988). The process of Raman scattering is characterized by a wavelength shift of the scattered radiation in respect to the exciting wavelength. The shift is uniquely associated with the internal transitions between the rotational–vibrational energy levels of the molecules (Inaba and Kobayasi, 1972; Inaba, 1976; Demtröder, 2005, 2013) and is used for identification of the scattering molecules. Because of the advantages of the high power laser source, the vertical detection range of the Raman lidars can extend to 7 km and throughout the troposphere (Whiteman et al., 1992; Vaughan et al., 1988; Goldsmith, 1998; Leblanc et al., 2008; Dinoev, 2009; Dinoev et al., 2013).

The Tibetan Plateau is a vast elevated plateau in the middle of the Eurasian continent with averaged elevation above 4500 m (m.s.l.), and it has an important role in the global and regional climate system (Kuwagata et al., 2001). The Tibetan Plateau lies at a critical and sensitive junction of four climatic systems: the Westerlies, the East Asian monsoon, the Siberian cold polar airflow and the Indian monsoon. The Tibetan Plateau has great impact on the water vapor budget of area around. The water vapor transportation based on the plateau–monsoon interaction affects the drought and flood of Asia and even the whole Northern Hemisphere (Park and Schubert, 1997; Ding and Wang, 2005; Li et al., 2011). A joint cloud experiment shows that very intense cloud activity continually exists over the Tibetan Plateau during the middle of the monsoon season, from the end of June to early September (Liu et al., 2015). Even though the altitude is high, a relatively wet condition is maintained over the Tibetan Plateau and the hydrological cycle is active during the monsoon season (Kuwagata et al., 2001).

The water vapor mixing ratio profile is usually monitored twice a day (00:00 and 12:00 UTC) by radiosondes. However, because of the limitation of the temporal resolution and the rather low measurement frequency, the water vapor mixing ratio data from radiosonde cannot satisfy the requirement of resolving fast running weather phenomena such as the development of convective boundary layer and passage of cold fronts (Dinoev, 2009), especially in the high-elevation area with strong radiation and convection. Moreover, the lack of the vertical profiles of water vapor mixing ratio make it difficult to obtain and analyze the vertical distribution of water vapor (Kuwagata et al., 2001). This paper introduces the lidar technique, an active sensing technique, to provide vertical profiles of water vapor mixing ratio with the advantages of high spatial resolution and updating rate.

Several lidars have been deployed for mountain-based atmospheric observations, where complex ambient conditions resulting from the high altitude above sea level need to be considered. One lidar system was set up and operated in 1973 at the Mauna Loa observatory (19.53° N, 155.58° W; 3400 m m.s.l.) (DeFoor and Robinson, 1987; DeFoor et al., 1992) for the detection of the eruption of the Philippine volcano Pinatubo firstly. A combined multi-wavelength Raman elastic-backscatter lidar system specially built for measurements in the EARLINET network (Larchevêque et al., 2002). The system was installed in 1999 at the Jungfraujoch Research Station (46.55° N, 7.98° E; 3580 m m.s.l.) to monitor the aerosol optical properties and water vapor. Since 2003, a powerful DIAL at the Schneefernerhaus high-altitude station next to the Zugspitze summit (Germany) (Vogelmann and Trickl, 2008; Klanner et al., 2010), located at 2675 m m.s.l., provides water vapor profiles in the entire free troposphere above 3 km with high vertical resolution and an accuracy of about 5 % up to 8 km. A micropulse backscatter lidar was operated in Naqu on the Tibetan Plateau to observe cirrus cloud top/bottom and optical depth from 19 July to 26 August 2011 (He et al., 2013).

In this paper, the observations of lidars during the third Tibetan Plateau Experiment of Atmospheric Sciences (TIPEX III) are described. The methodology of the water vapor mixing ratio, wind field and vertical water vapor flux are introduced in Sect. 2 and the results and case studies are provided in Sect. 3.

2 Lidar technology and methodology

The lidar observations in summer of 2014 as a part of the TIPEX III were performed in Naqu (31.48° N, 92.06° E; 4508 m m.s.l.), located in the north-central part of the Tibetan Plateau. During this campaign, the vertical profiles of water vapor mixing ratio were measured by a WAter vapor, Cloud and Aerosol Lidar (WACAL) based on the Raman lidar technique and the horizontal and vertical wind profiles were detected by a pulsed coherent doppler lidar (CDL). Moreover, the temperature, pressure and relative humidity were detected by radiosonde twice a day (00:00 and 12:00 UTC). Combining the data products of the three systems, the water vapor flux can be calculated. In the WACAL, it is essential to cool the air in this cabin since the laser chiller inside the cabin generates a lot of heat, which is harmful for the stable operation of the laser. The ventilation facility was operated with a high ventilation rate fan, which plays a very practical role in the high-elevation and low air pressure field experiment at the Tibetan Plateau. In addition, to avoid the electric arc breaking through the air under the condition of low pressure, the rated voltage of pump lamps in the laser oscillator and amplifiers were reduced, and therefore the heat load also decreased.

The principle and basic layout of WACAL is described in this section for the integrality and the detailed design is described in a separated paper (Wu et al., 2015). Figure 1 shows the schematic of WACAL. The laser transmitter of WACAL, Continuum Powerlite 9030, is a high peak power flash lamp-pumped Nd:YAG laser with three wavelengths of 354.7, 532 and 1064 nm and with the repetition

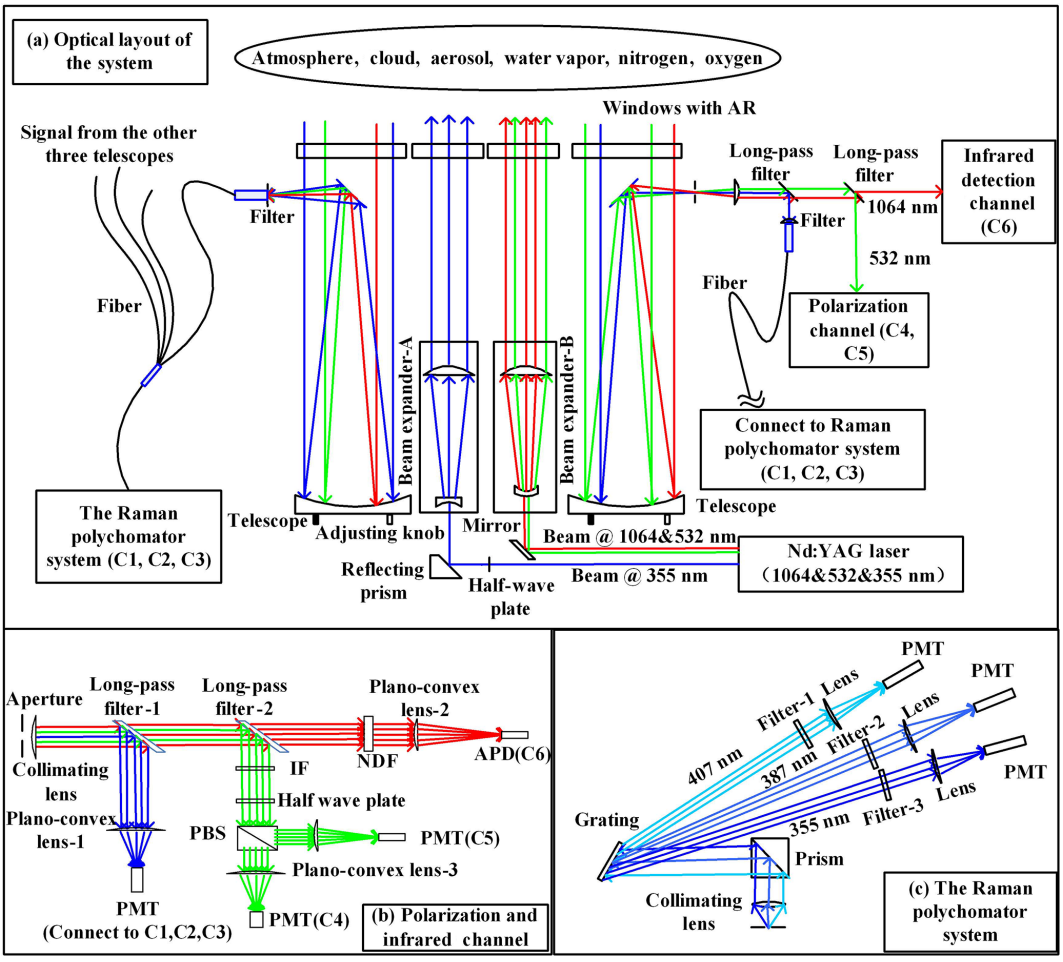

Figure 1. Schematic diagram and photos of WACAL.

rate of 30 Hz. The pulse energy is 410, 120 and 700 mJ, respectively. The flash lamp-pumped Nd:YAG laser transmitter generates light pulses at the wavelength of 1064 nm. Utilizing the second harmonic generator and third harmonic generator, the wavelengths of 532 nm (frequency doubled) and 354.7 nm (frequency tripled) are generated. With the residual light at wavelength 1064 nm, all these three beams are transmitted to the atmosphere simultaneously. The basic parameters are listed in Table 3. The light pulse with the wavelength of 354.7 nm is used for exciting nitrogen and water vapor molecule to Raman excitation of vibrational modes (Malinovskaya et al., 2004). The backscattered light at the wavelengths of 532 and 1064 nm is utilized for the detection of aerosol and cloud. For the purpose of the decreasing divergence angle, two beam expanders are designed. As shown in Fig. 1, the transmitter includes a laser, one half-wave plate, one reflecting prism, one mirror, two beam expanders and two windows with anti-reflective coating. The expanded laser beams with 90 mm diameter transmit into the atmosphere on an axis closed to the receiver axis.

After a laser pulse is transmitted to the atmosphere, molecules and particles scatter the light in all directions. A portion of the light is scattered backwards to the lidar that is collected by telescopes and then transmitted to the detection system. In order to increase the amount of collected light, this system uses four Newtonian telescopes with the diameter of 300 mm and the focal length of 1524 mm, forming a telescope array with an equivalent receiver aperture of about 610 mm. The primary mirror of Newtonian telescope is a parabolic mirror while the secondary mirror is a plane mirror. The design of the array has better practicability for detecting the signal from near field and far field. Moreover, it takes the collection efficiency of the strong elastic backscatter light and the weak Raman backscatter light into consideration. This design makes the system easy to transport and suitable for field experiments. However, it also makes the system more complicated to align the telescope and to determine the overlap function.

Collected by the telescope array, the scattered light is transmitted into five fibers, including four far-field fibers and one near-field fiber. Considering the overlap function and the

Table 1. Branches of the rotational–vibrational Raman spectrum.

$\Delta\upsilon$	ΔJ	Branch
$\pm1, \pm2$	-2	O branch
$\pm1, \pm2$	0	Q branch
$\pm1, \pm2$	$+2$	S branch

Table 2. The shift of wave number of nitrogen and water vapor.

Molecule	Excitation wavelength	Δk $\Delta\upsilon = 1$, $\Delta J = 0$	The center of the Q branch
Nitrogen	354.7 nm	2330.7 cm^{-1}	386.7 nm
Water vapor	354.7 nm	3651.7 cm^{-1}	407.5 nm

collection efficiency of near-field signal, the near-range fiber is designed specially (Wu et al., 2015).

Here the rotational–vibrational Raman spectrum of nitrogen and water vapor are explained. According to the selection rule for vibrational transitions (Inaba and Kobayasi, 1972; Inaba, 1976; Demtröder, 2005, 2013), the change of the vibrational quantum number is $\Delta\upsilon = 0, \pm1, \pm2, \ldots$. However, the sublevels cannot be ignored. The change of the rotational quantum number ΔJ obeys to the transition selection rule of $\Delta J = 0, \pm2$. In turn, the $\Delta\upsilon$ and ΔJ can describe the rotational resolved molecular transitions. So because of the presence of sublevels, several branches of rotational–vibrational Raman spectrum can be detected as Table 1 shows.

All lines in the Q branch lie very close to each other and are not resolved except with extremely high-resolution spectroscopy. The S branch ($\Delta\upsilon = 1, \Delta J = +2$) and O branch ($\Delta\upsilon = 1, \Delta J = -2$) are well separated in energy and appear as sidebands on the either side of the Q branch (Inaba and Kobayasi, 1972). The cross section of nitrogen in Q branch is about $10^{-30}\,\mathrm{cm}^2\,\mathrm{sr}^{-1}$, which is 2 orders of magnitude bigger than the cross section in S and O branch (about $10^{-32}\,\mathrm{cm}^2\,\mathrm{sr}^{-1}$). In Table 2, the shift of wave numbers Δk corresponding to $\Delta\upsilon = 1, \Delta J = 0$ of nitrogen and water vapor are listed. In this work, the Q branch ($\Delta\upsilon = 1, \Delta J = 0$) is applied for the detection. Moreover, by using the narrowband interference filters, the cross-talk noise of S and O branch backscatter light is highly suppressed.

Since the Raman scattering signal is 2–3 orders of magnitude weaker than Rayleigh scattering signal, the detection of the Raman signal at wavelength of 386.7 and 407.5 nm is more difficult because of the much lower signal-to-noise ratio (SNR). As discussed above, a telescope array with the relatively large equivalent aperture of 610 mm is used to increase the efficiency of optical receiver. Four fibers are mounted at the focus of the telescopes for the coupling of the signal. The core diameter of the fiber is 200 microns and the numerical aperture is 0.22, which also serves as a field stop. Through the coupling of fibers, the Raman signal is delivered to the spectrometer which separate nitrogen Raman signal and water vapor Raman signal. The Mie and Rayleigh scattering signal at 532 and 1064 nm are transmitted to the polarization channel and the infrared channel, respectively, to retrieve the depolarization ratio, extinction coefficient and cloud height, which are not described in detail in this paper.

The schematic diagram of Raman channel is shown in Fig. 1c, in which the transmitter, receiver and spectrometer are illustrated in detail. For the purpose of avoiding the interference of the elastic backscatter signal, band-pass filters are used. The central wavelength of the filters is 390 nm and the FWHM is 44.6 nm. The transmission between 370 and 410 nm is greater than 93 % and the optical density (OD) is greater than 5 for light at the wavelength of 354.7 and 532 nm.

When the signal is transmitted to the spectrometer, the light is dispersed and then collimated by the convex lens with the focal length of 50.0 mm. Reflected by the reflecting prism, the parallel light then arrives at the grating. The groove density of the grating is 1302 L mm^{-1} and the blaze is 400 nm. The Raman scattering signal from nitrogen and water vapor separate and go in different directions to the photomultiplier tubes (PMTs) because of the grating diffraction. Then the additional narrow band filters are used before the PMT to suppress the interference from the elastic scattering and the stray light. The central wavelengths are 407.5 ± 0.1, 386.7 ± 0.1 and 354.7 ± 0.08 nm for filter 1, filter 2 and filter 3, respectively. The FWHM of all filters is 0.5 ± 0.10 nm and the peak transmittance is greater than 50 % and provides high rejection OD of 5 outside the band from 200 to 1200 nm. Note that together with the filters at the incident end of the fibers, the total OD in the Raman channel is > 10 to eliminate the interference from the elastic backscatter signal. The scattering signals are then focused by a plano-convex lens with a focal length of 100 mm. Finally, the scattering signals are acquired by the PMTs, which are mounted at the focal point of the plano-convex lens. The specifications of the optical elements of this channel are shown in Table 3. The Raman lidar equation can be described as Eq. (1) (Dinoev, 2009):

$$P(z,\lambda_\mathrm{R}) - P_\mathrm{BG} = \quad (1)$$
$$P_0(\lambda_\mathrm{L})\Delta z \frac{A_0 O(z)}{z^2}\xi(\lambda_\mathrm{R})\beta^\pi_\mathrm{R}(z,\lambda_\mathrm{R})T^\mathrm{up}(z,\lambda_\mathrm{L})T^\mathrm{down}(z,\lambda_\mathrm{R}),$$

$$T^\mathrm{up}(z,\lambda_\mathrm{L}) = \exp\left[-\int_{z_0}^{z}\alpha(z',\lambda_\mathrm{L})\mathrm{d}z'\right] \quad (2)$$

$$T^\mathrm{down}(z,\lambda_\mathrm{R}) = \exp\left[-\int_{z}^{z_0}\alpha(z',\lambda_\mathrm{R})\mathrm{d}z'\right],$$

where $P_0(\lambda_\mathrm{L})$ is the laser pulse energy at a wavelength of λ_L, P_BG is the background signal and noise, Δz is the range resolution, A_0 is the aperture of the telescope, $O(z)$ is the overlap of the system at height of z, $\xi(\lambda_\mathrm{R})$ is the receiving efficiency

Table 3. System specification of the Raman channel of the WACAL. CWL stands for central wavelength; OD refers to optical density.

System	Specification	
Laser	Wavelength (nm)	354.7
	Pulse energy (mJ)	410
	Repetition rate (Hz)	30
	Divergence (mrad)	0.5
	Pulse width (ns)	3–7
	Stability (±%)	4.0
Beam expender	Amplification factor	×10 at 355 nm
Telescope	Aperture (mm)	304.8
	Focal length (mm)	1524
Fiber	Aperture (μm)	200
Polychromator	Collimating lens	Focal length: 50 mm
	Grating	D: 1302 L mm
		Blaze: 400 nm
	Filter 1	CWL: 407.5 ± 0.1 nm,
		FWHM: 0.5 ± 0.10 nm
		Peak %T: 50 %, OD5
	Filter 2	CWL: 386.7 ± 0.1 nm,
		FWHM: 0.5 ± 0.10 nm
		Peak %T: 50 %, OD5
	Filter 3	CWL: 354.7 ± 0.08 nm,
		FWHM: 0.5 ± 0.10 nm
		Peak %T: 50 %, OD5
	Lens	Focal length: 100 mm
Photomultiplier tube	Photocathode area size (Dia. mm)	0.8
(Hamamatsu H10721P-110)	Cathode radiant sensitivity	∼ 100 mA W^{-1} at 355 nm
	Wavelength (peak, nm)	400
Data acquisition system	Temporal resolution (ns)	25
(Licel transient recorder)	Range resolution (m)	3.75
	Maximum counting rate (MHz)	250

at the given wavelength λ_R, $\beta_R^{\pi}(z,\lambda_R)$ is the backscatter coefficient at λ_R at height of z, and $\alpha(z,\lambda_L)$ and $\alpha(z,\lambda_R)$ are the extinction coefficient at wavelengths of λ_L and λ_R, respectively. $T^{up}(z,\lambda_L)$ and $T^{down}(z,\lambda_R)$ are the atmospheric transmission at λ_L and λ_R, respectively.

According to Eq. (1), the backscatter signals of N_2 and H_2O are obtained as $P(z,\lambda_{N_2})$ and $P(z,\lambda_{H_2O})$. The water vapor mixing ratio can be calculated by Eq. (3):

$$w(z) = C\frac{P(z,\lambda_{H_2O})}{P(z,\lambda_{N_2})}\Delta T(\lambda_{N_2},\lambda_{H_2O},z), \tag{3}$$

where C is the calibration constant and can be obtained by the validation of lidar data and radiosonde data. $\Delta T(\lambda_{N_2},\lambda_{H_2O},z)$, contributed by molecular and aerosol extinction, is the differential atmospheric transmission at nitrogen and water vapor Raman wavelengths and is calculated by Eq. (4):

$$\Delta T(\lambda_{N_2},\lambda_{H_2O},z) = \exp\left(-\int_{z_0}^{z}\left[\alpha\left(z',\lambda_{N_2}\right)-\alpha(z',\lambda_{H_2O})\right]\mathrm{d}z'\right). \tag{4}$$

$\alpha(z',\lambda_{N_2})$ and $\alpha(z',\lambda_{H_2O})$ are calculated by Raman method (Ansmann et al., 1992). The calibration constant is retrieved using linear regression to a vertical water vapor mixing ratio profile obtained by a reference radiosonde of GTS1 type (Qiyun et al., 2012). The radiosonde provides temperature accuracy of ±0.2 °C, relative humidity accuracy of ±5 % and pressure accuracy of ±1 hPa. Additionally, the pressure and relative humidity profiles are also obtained. Equation (5) is used to obtain a mixing ratio profile from radiosonde data. In this equation, the temperature, pressure and

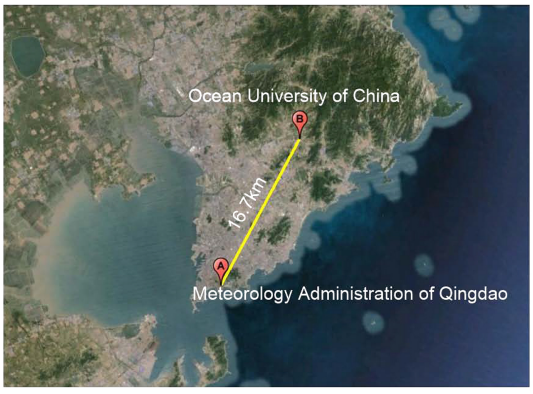

(a)

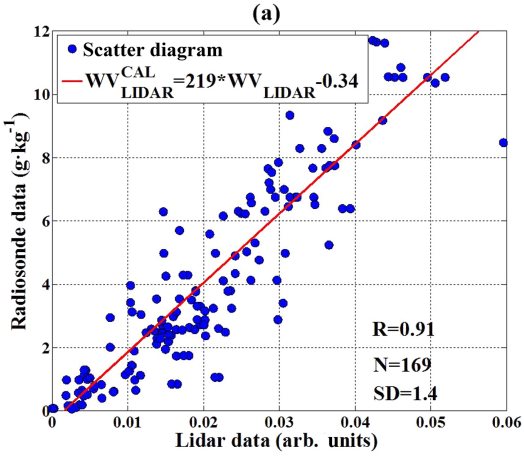

(b)

Figure 2. (a) Distance between sites of WACAL and radiosonde; **(b)** regression of WACAL mixing ratio profile to radiosonde measurement.

relative humidity profiles are used and the mixing ratio, WR (g kg^{-1}), is then estimated.

$$\mathrm{WR} = \varphi \cdot S = \varphi \cdot \frac{0.622 \cdot P_\mathrm{s}(T)}{P - 0.378 \cdot P_\mathrm{s}(T)}, \quad (5)$$

where φ is the relative humidity, S is the specific humidity, P is the atmospheric pressure, and P_s is the saturated vapor pressure (mb) at temperature T (°C) and can be calculated by the Arden Buck equation (Buck, 1981), as Eq. (6) shows:

$$P_\mathrm{s}(T) = 6.1121 \cdot \exp\left(\left(18.678 - \frac{T}{234.5}\right) \cdot \left(\frac{T}{257.14 + T}\right)\right). \quad (6)$$

The calibration constant for this comparison is shown in Fig. 2. The lidar water vapor mixing ratio (W_Lidar) profile is calculated according to Eq. (3) with a calibration constant set to 1. We assume that the relationship between lidar data $W_\mathrm{Lidar} = \Delta T(\lambda_{\mathrm{N}_2}, \lambda_{\mathrm{H}_2\mathrm{O}}, z) \cdot \frac{P(z,\lambda_{\mathrm{H}_2\mathrm{O}})}{P(z,\lambda_{\mathrm{N}_2})}$ and radiosonde data W_Sonde to be as in Eq. (7):

$$W_\mathrm{Sonde} = C \cdot W_\mathrm{Lidar} + D, \quad (7)$$

Table 4. Period of time of the simultaneous observations.

May 2014	12	21	22	26	27	28	29	31
June 2014	3	4	5	6	7	8	9	10
	12	14	15	16	17	18	20	23

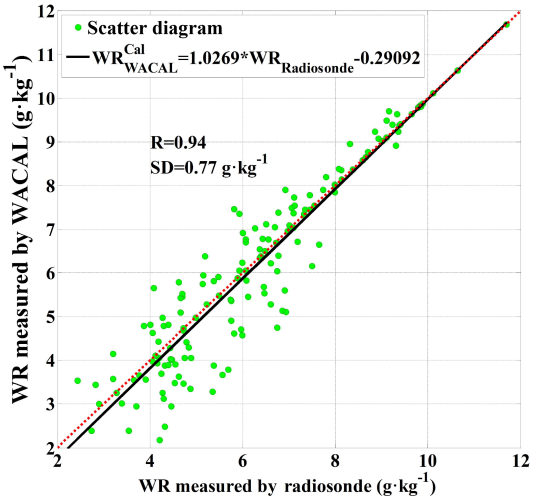

Figure 3. Validation of the calibrated water vapor mixing ratio (red dashed line is 1 : 1 curve and black line is fitting curve).

where C is the calibration constant and D is the offset. Before the field campaign in the TIPEX III program, the water vapor profiles of the WACAL were compared with those of radiosonde at the campus of Ocean University of China in Qingdao. Since the radiosondes were launched every day at 00:00 and 12:00 UTC, the lidar measurements covered the time period for the purpose of validation. The radiosondes were launched at the site of Meteorological Administration of Qingdao (36.07° N, 120.33° E), while the WACAL was deployed at Laoshan campus, Ocean University of China (36.16° N, 120.49° E). As Fig. 2a shows, the distance between these two sites is 16.7 km. In Table 4, the time periods of the simultaneous observations by radiosonde and WACAL is provided.

Using the linear regression model, the water vapor mixing ratio profiles from the lidar and the radiosondes are fitted. The slope using the linear regression fitting is a direct estimation of the lidar calibration constant C. According to Fig. 2b, C is determined as 219. D is the offset and determined as −0.34. As a result from the different observation stations of the WACAL and radiosonde and the WACAL system error, the offset exists. The correlation coefficient of measurements by two systems is 0.91. The standard deviation is 1.4 and the number of samples is 169. With the calibration the water vapor mixing ratio can be rewritten as Eq. (8):

$$W_\mathrm{Lidar}^\mathrm{Cal} = 219 \cdot W_\mathrm{Lidar} - 0.34. \quad (8)$$

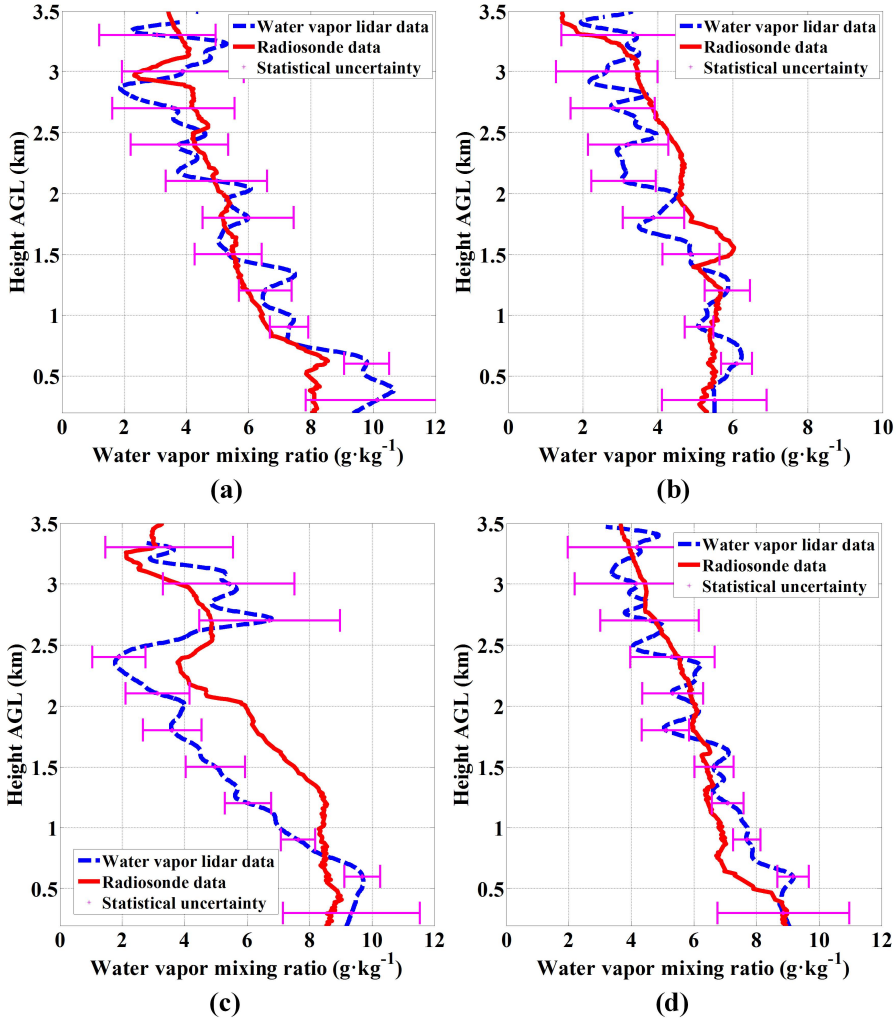

Figure 4. Water vapor mixing ratio case studies: **(a)**, **(b)**, **(c)** and **(d)** measured in Naqu on 11, 15, 18 and 22 July 2014, respectively.

2.1 Observation results and discussion

Atmospheric observations were performed in Naqu (31.48° N, 92.06° E; 4508 m m.s.l.) in the Tibetan Plateau from 10 July to 16 August 2014 by utilizing the WACAL and other lidars.

Atmospheric backscatter signals are recorded using both analog-to-digital convertor and photon counting technique. However, data acquisition by the photon counting method is possible only when the photons are individually distinguishable (Whiteman et al., 1992). In other words, because of the saturation effect and the bandwidth limitation of PMTs, the response of photon counting system is nonlinear. Consequently, nitrogen and water vapor scattering signals have to be corrected by the equation

$$P_{\text{real}} = \frac{P_{\text{meas}}}{1 - \tau \cdot P_{\text{meas}}}, \quad (9)$$

where P_{real} is the actual number of photons detected by PMTs, P_{meas} is the measured counts and τ is the resolving time of the discriminator counter combination of PMTs, which is also known as the dead time of the photon counting technique.

In order to validate the calibration equation, the scatter diagram of the measurements by calibrated lidar method and radiosonde in Naqu is shown in Fig. 3.

Note that the correlation coefficient is up to 0.9354 and mean deviation is 0.77 g kg^{-1}. As a conclusion, the calibration of WACAL measurement can give a reasonably accurate estimate of water vapor profile for the routine observation. Here we provide some case studies in Fig. 4 for the discussion. Several intercomparisons of lidar-derived vertical profiles with radiosonde measurements are presented (Fig. 4) as well as time serials of water vapor mixing ratio in Naqu from 10 July to 16 August 2014 (Fig. 5).

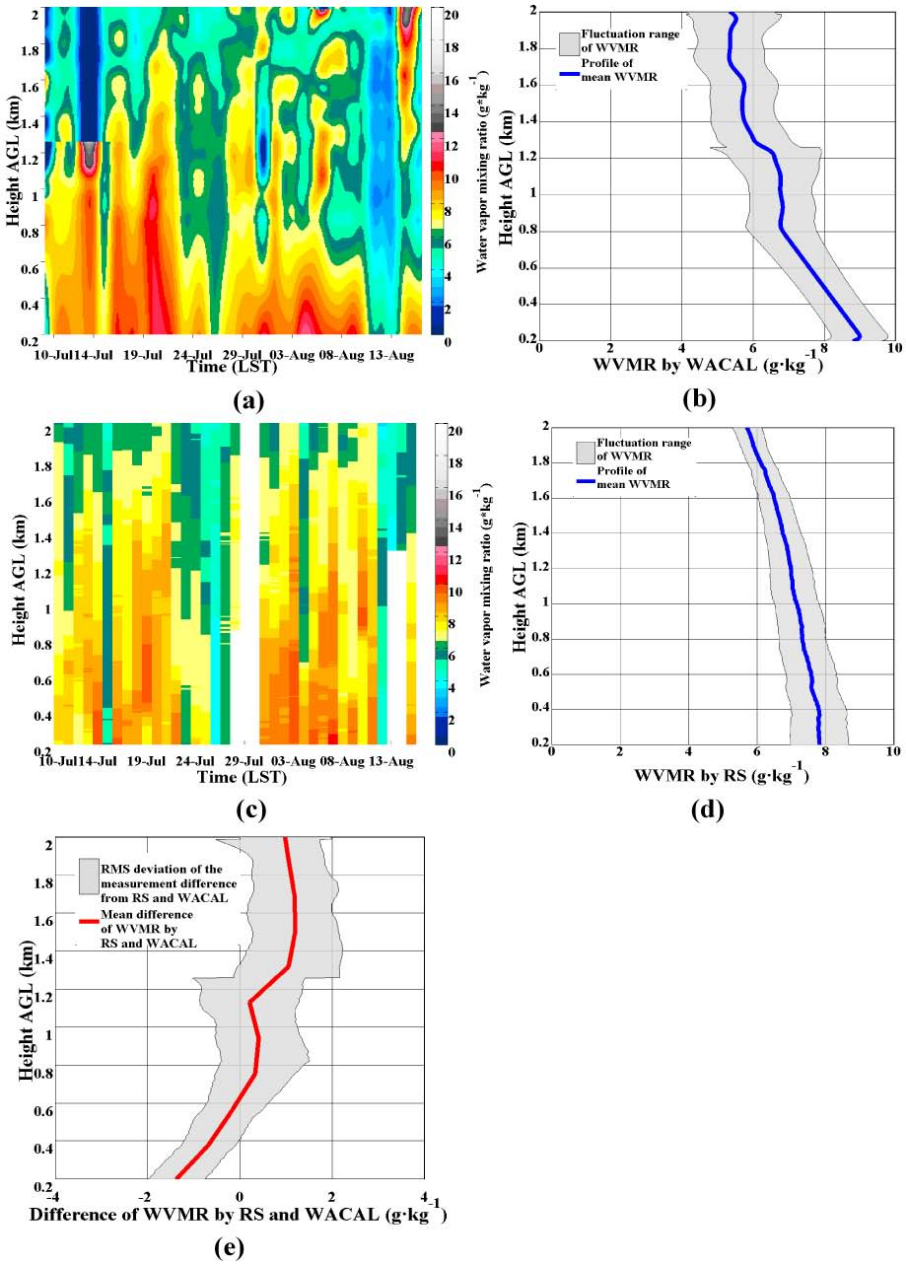

Figure 5. (a) Time serials of water vapor mixing ratio at 21:30 LST from 10 July to 16 August measured by WACAL; **(b)** profile of mean water vapor mixing ratio and fluctuation range of water vapor mixing ratio from 10 July to 16 August measured by WACAL; **(c)** time serials of water vapor mixing ratio at 21:30 LST from 10 July to 16 August measured by radiosonde (RS); **(d)** profile of mean water vapor mixing ratio and fluctuation range from 10 July to 16 August measured by RS and **(e)** mean difference of water vapor mixing ratio measured by WACAL and RS and the corresponding root mean square deviation.

In Fig. 4, the blue dashed line indicates the water vapor mixing ratio measured by lidar and the horizontal line shows the statistical uncertainty of the water vapor mixing ratio. The red line shows the data which are obtained from the operational radiosondes. In these figures, the water vapor mixing ratio with relative errors larger than 65 % is removed. From these four figures, one dry layer can be seen at about 2.8 to 3 km in Fig. 4a and one distinct wet layer can be found at about 2.5 to 3.2 km in Fig. 4c. In Fig. 4b and d, the water vapor mixing ratio gradually decreased as height increase. All of the water vapor mixing ratio profiles is averaged every 90 min and the range resolution is 75 m.

According to the profiles of water vapor mixing ratio, the observation results of the lidar and operational radiosonde

have a good consistency. Since the nitrogen concentration at elevation of 4508 m is about 42 % lower than that at sea level, the density and the backscatter coefficient of water vapor is also much lower in Naqu with high elevation over 4500 m. Furthermore, because the background light in Naqu was still strong at 20:00 LST (UTC + 8) and the strong solar radiation in ultra violet is caused by shallow atmosphere, it also brings in errors in the water vapor mixing ratio measurement. To ensure the accuracy of the measurement, the WACAL measured the water vapor profiles from 21:30 LST, which is 1.5 h later than the measurement of radiosonde. The measuring time difference may be the main error source of observation in Naqu.

In Fig. 5, the water vapor mixing ratio measured by the WACAL and the radiosonde is presented. The time serials of water vapor mixing ratio from these two systems are provided in Fig. 5a and c, respectively. The trend of $W_{\text{Lidar}}^{\text{Cal}}$ is shown and two dry or low water vapor content time periods are found. Figure 5b and d provide the profiles of mean water vapor mixing ratio and fluctuation range of water vapor mixing ratio from 10 July to 16 August measured by WACAL and radiosonde. Mean difference of water vapor mixing ratio measured by WACAL and radiosonde and the corresponding root mean square deviation, which are shown in Fig. 5e, indicate that the water vapor mixing ratio measured by WACAL is about 0.7 g kg^{-1} smaller than that measured by radiosonde. This result corresponds to the standard deviation from Fig. 3 but can only partly explain the difference of water vapor mixing ratio between Fig. 5a and c. The water vapor mixing ratio difference above 1 km a.g.l. can be explained by the WACAL and radiosonde measurement time difference of 1.5 h. Another possible reason of this difference might be the instrumental bias.

In the following section, the error analysis of the signal and results are discussed. To evaluate detection performance of the lidar system, the SNR is taken into consideration, which can be described as Eq. (10) (Papayannis et al., 1990; Pelon and Mégie, 1982):

$$\text{SNR}_i = \frac{P_i}{\sqrt{P_i + P_{\text{bi}}}}, \tag{10}$$

where P_i is the corrected power of backscatter signal without optoelectronic noise, and P_{bi} is the solar background signal and noise.

Moreover, from Eq. (3), the relative error δ_{RE} can also be calculated by Eq. (11):

$$\delta_{\text{RE}} = \frac{1}{\sqrt{N}}\left(\frac{1}{\text{SNR}_1^2} + \frac{1}{\text{SNR}_2^2}\right), \tag{11}$$

where N is the number of profiles used for averaging. SNR_1 and SNR_2 are the signal-to-noise ratios of nitrogen and water vapor Raman signal, respectively.

Here we will present one case study of the SNR and δ_{RE}. In Fig. 6, the SNR and relative statistical uncertainty are analyzed. Because of the limitation of the lower water vapor

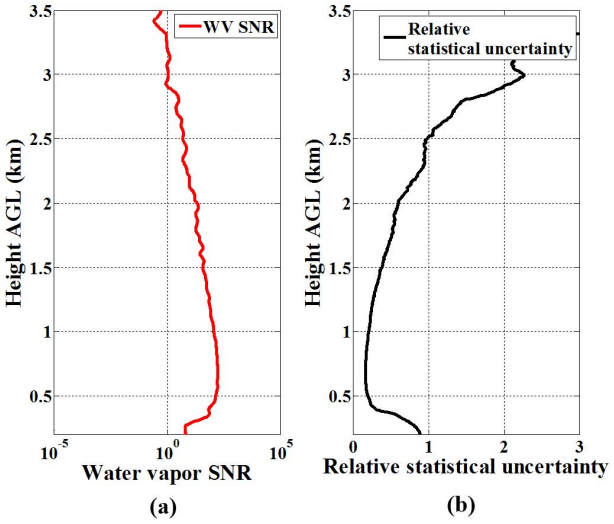

Figure 6. The SNR of water vapor Raman signal and the relative statistical uncertainty of water vapor mixing ratio at nighttime of 15 July 2014.

content, the acceptable detection range is 2 km. The greatest SNR for water vapor in this observation is 220.

From Figs. 4 and 5, it is worth noting that the water vapor mixing ratio is several times higher than the global average and still at least 2 times higher than in a tropical atmosphere at corresponding altitudes. According to the historical report from the local meteorological observatory, the average annual precipitation in Naqu is 380–420 mm, 80 % of which is in summer and autumn. As we well know, the Tibetan Plateau not only feed the most of Asia's major rivers, it also holds scattered numerous lakes. Naqu is located in the north central part of the Tibetan Plateau that is a sub-frigid, semi-arid, monsoon climate zone, with the largest lake, Nam Co Lake, in the Tibetan Plateau. The high water vapor content may mainly result from the combination of the monsoon activities and the strong evaporation from nearby plateau lakes because of strong solar radiation and ground heating. The backward trajectory analysis based on the HYSPLIT model (Draxler and Rolph, 2003; Rolph, 2003) from NOAA leads to the possible sources of the water vapor. Four backward trajectories simulated by the HYSPLIT model, ending at 21:00 LST on 11, 15, 18 and 22 July 2014, are provided in Fig. 7. The black star represents the observation station of lidar in Naqu. On the basis of the trajectories, the high water vapor content partly resulted from the advection from the Southeast Asian warm pool region. Furthermore, based on our observations by the CDL, the eastern wind dominates the wind field during the field experiments in Naqu, which may indicate the influence of the Asian monsoon. To conclude, the observed high water vapor mixing ratio is likely effected by the combination of the moisture from Southeast Asian warm pool region and Asian monsoon.

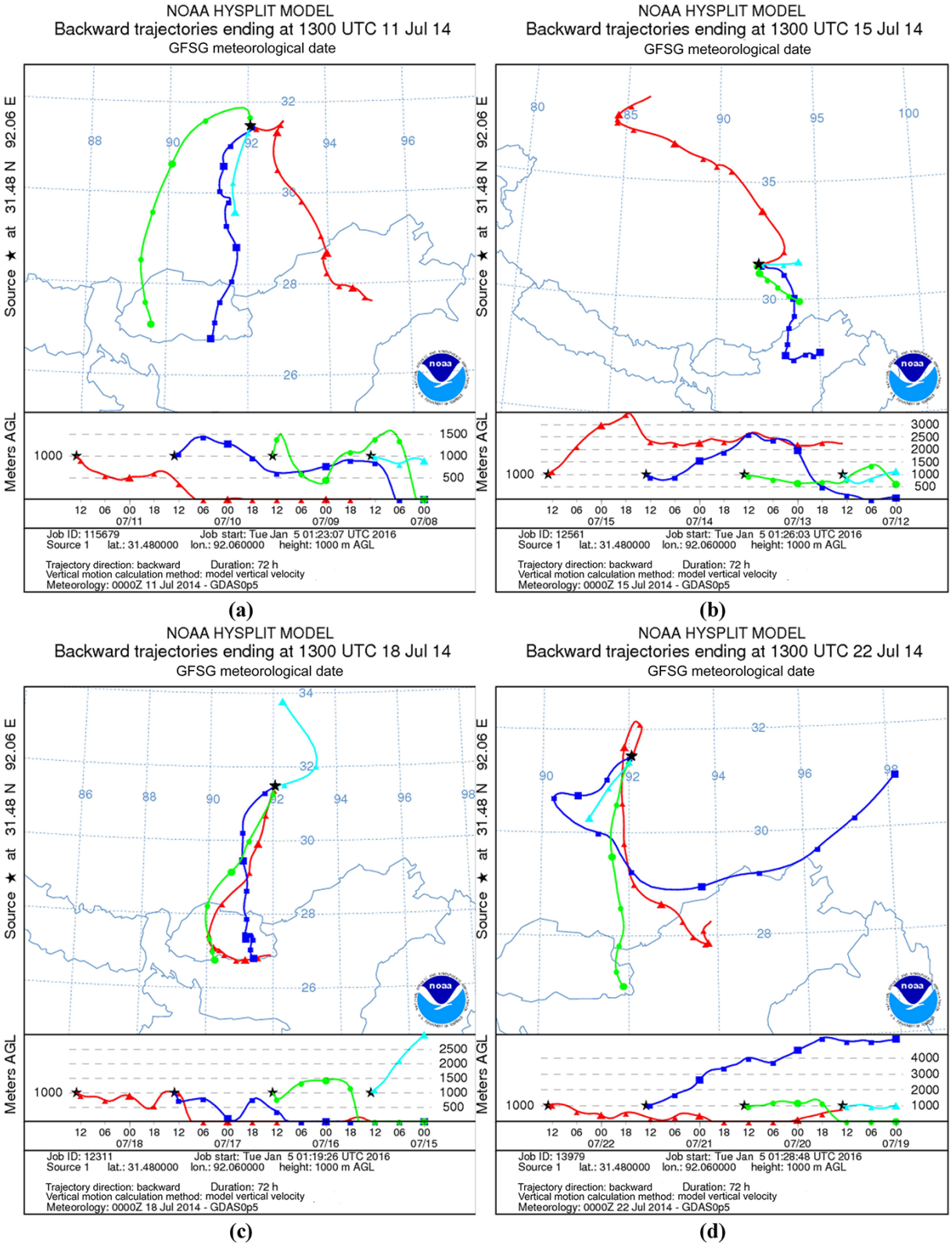

Figure 7. Backward trajectories ending at 21:00 LST on **(a)** 11, **(b)** 15, **(c)** 18 and **(d)** 22 July 2014, simulated by the HYSPLIT model.

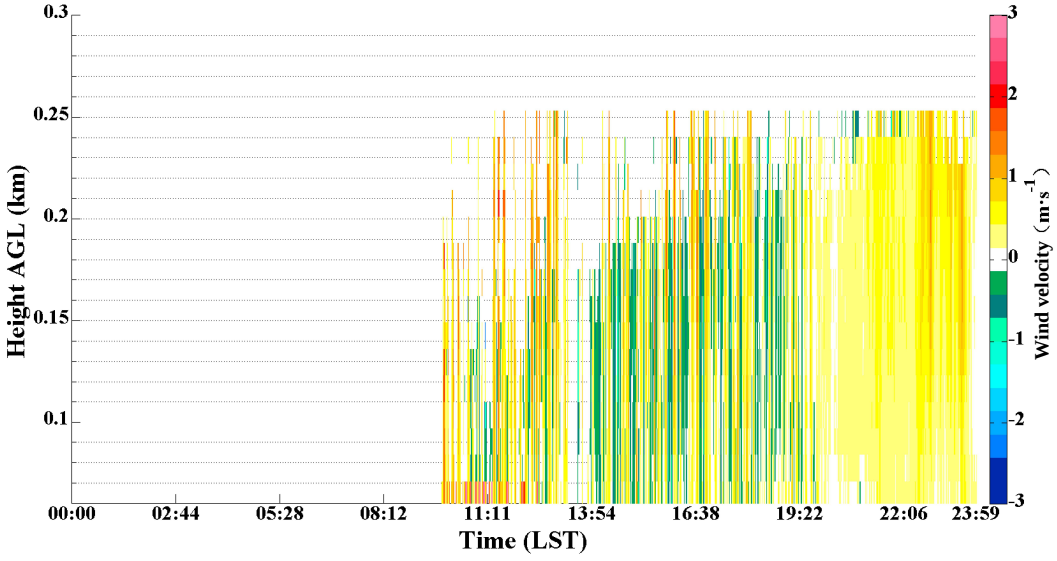

Figure 8. Time serials of vertical wind velocity from 00:00 to 23:59 LST on 15 July 2014.

In addition to the water vapor content measurements, the wind profiles were measured by a compact CDL to calculate the water vapor flux. The CDL takes advantage of the fact that the frequency of the backscatter signal is shifted compared to the local-oscillator light because of the Doppler effect which occurs from backscattering of aerosols. The details of the CDL system is described in a separated paper (Wu et al., 2014). The Doppler shift in the frequency of the backscattered signal is analyzed to calculate the line-of-sight (LOS) velocity component of the air motion. The Doppler shift f_D can be obtained as follows:

$$f_D = \frac{2|\boldsymbol{V}_{LOS}|}{\lambda}, \quad (12)$$

where $\boldsymbol{V}_{LOS}$ is the LOS velocity and λ is the laser wavelength, 1550 nm in this lidar system.

Once the LOS velocities in four directions, $\boldsymbol{V}_{LOS,E}$, $\boldsymbol{V}_{LOS,W}$, $\boldsymbol{V}_{LOS,S}$ and $\boldsymbol{V}_{LOS,N}$, are measured, the vertical wind speed can be calculated by Eq. (13) (Cariou, 2011):

$$\boldsymbol{V}_{ver} = \frac{1}{4\sin\theta}(\boldsymbol{V}_{LOS,E} + \boldsymbol{V}_{LOS,W} + \boldsymbol{V}_{LOS,S} + \boldsymbol{V}_{LOS,N}), \quad (13)$$

where θ is the elevation angle.

With the concurrent observations of the profiles of water mixing ratio and vertical velocity, the vertical water vapor flux, $\text{flux}_{WV,ver}$, can be calculated by Eq. (14) (Giez et al., 1999):

$$\text{Flux}_{WV,ver}(T) = \overline{W_{Lidar}^{Cal} \cdot |\boldsymbol{V}_{ver}|}, \quad (14)$$

where W_{Lidar}^{Cal} and $\boldsymbol{V}_{ver}$ are the time serials of the mean vertical air movements and moisture transports in the water vapor mixing ratio and the vertical wind speed. The bar represents the temporal average over the time interval T. For the consistency of the symbols, the symbols in Eq. (14) are different from the original paper (Giez et al., 1999).

Although the water vapor mixing ratio was only measured in the nighttime during the TIPEX III, a long-time serial observation of vertical wind velocity is still important to recognize the unique atmospheric characteristics and heating power over the Tibetan Plateau. From the wind observation, the turbulence, updraft and downdraft at different time periods during a day can be detected and analyzed. One case study on 15 July 2015 is provided in Fig. 8. From 00:00 to 09:27 LST, because of the low temperature and rare human and industrial activities, the boundary layer in the Tibetan plateau is too low, under some circumstances, to be detected at nighttime by the CDL with a minimum detection limit of 90 m. During the daytime, the high turbulence can be found and the value of the vertical wind velocity is between $\pm 1\,\text{m s}^{-1}$. However, the turbulence decreased in nighttime and the vertical wind velocity is between 0 and $1\,\text{m s}^{-1}$, which indicates that the updraft of the atmosphere due to the difference in temperature between the heated ground and the cooled air in nighttime.

One case sturdy about vertical wind velocity and vertical water vapor flux on 15 August 2014 is presented in Figs. 9 and 10. The fluxes are for a case at night with large-scale nonturbulent upward transport of moisture. Figure 9a shows the time serials of range correction backscattering signal measured by the WACAL and Fig. 9c is the time serials of the vertical wind velocity profiles of 83 min obtained from the CDL. Then we can calculate the vertical water vapor flux from the water vapor mixing ratio (Fig. 9b) and the vertical wind velocity (Fig. 9c). The original temporal resolution (Δt) and the spatial resolution (Δr) of the vertical wind ve-

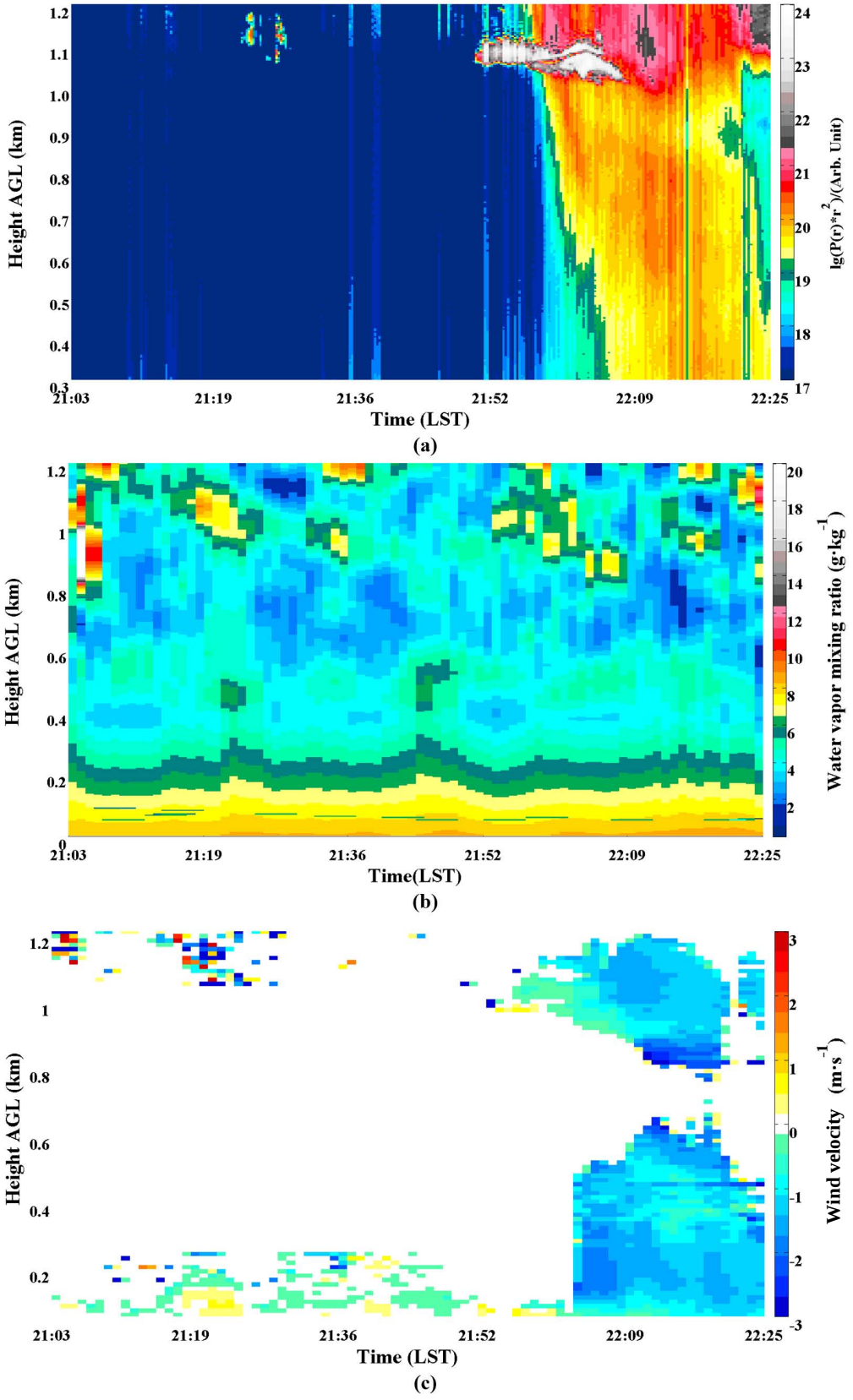

Figure 9. (a) Time serials of range correction signal measured by WACAL from 21:03 to 22:25 LST; **(b)** time serials of combined water vapor mixing ratio measured by WACAL and radiometer from 21:03 to 22:25 LST; **(c)** time serials of vertical velocity profile from 21:03 to 22:25 LST.

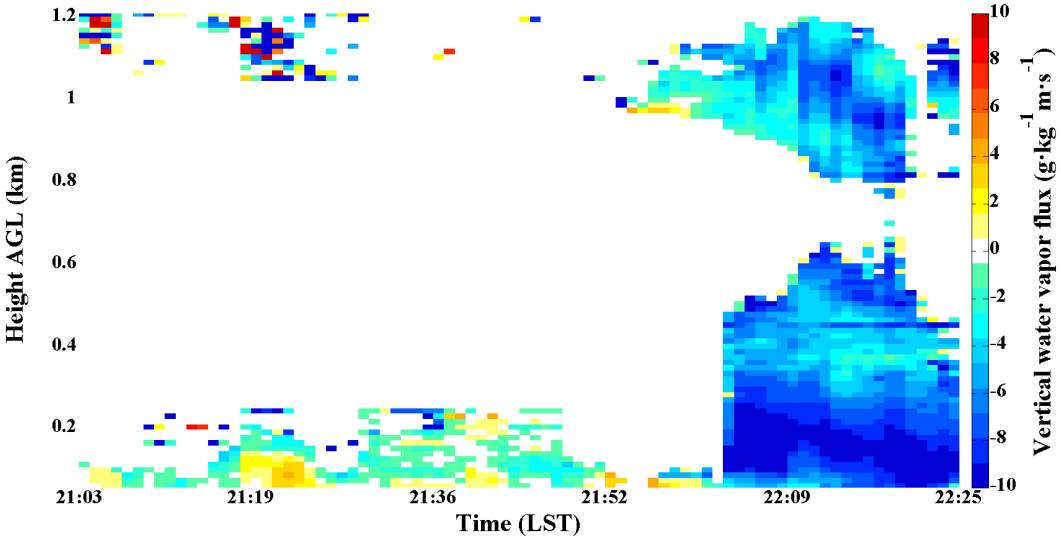

Figure 10. Time serials of vertical water vapor flux from 21:03 to 22:25 LST.

locity is 22 s and 13 m, respectively. And the original Δt and Δr of the water vapor mixing ratio is 16 s and 3.75 m, respectively. In order to capture the turbulent processes, the simultaneous and concurrent observations of the WACAL and CDL should have the same sampling rate and the high resolution. Figure 9c shows that the temporal scale of the wind fluctuations is a few minutes and the atmosphere is not turbulent in the analysis period but non-turbulent transport took place. Obviously, larger-scale circulations were responsible for longer-lasting local updrafts in this case. The sampling should be fine with 1 min resolution of the water vapor data in this case. Therefore, the Δt and Δr of WACAL and CDL are adjusted to be 1 min and 13 m, respectively. For this purpose, within a 1 min period, three profiles of original water vapor mixing ratio (48 s) and two profiles of original vertical wind velocity (44 s) are integrated, respectively, to represent the corresponding water vapor mixing ratio and vertical wind velocity of this minute.

The time serials of water vapor mixing ratio shown in Fig. 9b indicate that the water vapor content inside clouds located at the height of 0.82 to 1.2 km at time period from 21:52 to 22:06 LST is $5.77 \pm 0.41\,\mathrm{g\,kg^{-1}}$, higher than that of the ambient atmosphere. In Fig. 10, the mean vertical air movements and moisture transports are provided. It can be seen in Fig. 10a that it started to rain at about 22:00 LST. It is also worth mentioning that the water vapor transported both by the updraft and downdraft and the flux was about $0.78 \pm 1.38\,\mathrm{g\,kg^{-1}\,m\,s^{-1}}$ between 21:03 and 22:00 LST before the rain. Meanwhile, in the process of rain, the water vapor inside the clouds kept transporting downwards and the flux is about $-3.91 \pm 1.74\,\mathrm{g\,kg^{-1}\,m\,s^{-1}}$. Note that because of the coverage of raindrops on the optical windows of WACAL, the water vapor mixing ratios measured between 22:05 and 22:10 LST were removed by data quality control. Nevertheless, a small-scale water vapor cycling can be recognized, in which the ascending and descending of the water vapor were monitored.

3 Summary

In this study, we have presented atmospheric profile observations based on the lidar technique during the TIPEX III in 2014 in Naqu. With the help of the WACAL and CDL, we observed the water vapor mixing ratio and vertical wind velocity profiles, as well as the vertical water vapor flux in the Tibetan Plateau, and obtained information about the atmospheric conditions. The key findings of this study are listed below.

The calibration and validation of water vapor mixing ratio measurement have been completed. In the process of the calibration, we found a correlation coefficient of 0.91 between the measurements of lidar and radiosondes. The validation experiment shows a correlation coefficient of 0.94 and the standard deviation of $0.77\,\mathrm{g\,kg^{-1}}$. Considering the distance and measurement time difference between the lidar and radiosondes, the deviation is acceptable, indicating that the lidar as a useful remote sensing tool can be used for high temporal and spatial monitoring of water vapor mixing ratio profile.

Water vapor mixing ratio profiles in Naqu, the Tibetan Plateau, were measured, for the first time to our knowledge, and some case studies are provided in this paper. The observations were operated in Naqu from July to August 2014. The water vapor content in the Tibetan Plateau in summer was relatively high, mainly because of the monsoon and moisture evaporating from nearby lakes. The moist air from the Southeast Asian warm pool region may be another source of

the water vapor. According to the wind observation by the coherent Doppler lidar, the eastern wind dominated in summer in the Naqu area, indicating the influence of the Asian monsoon.

According to the time serials of water vapor mixing ratio at 21:30 LST from 10 July to 16 August 2014, the development of water vapor mixing ratio was monitored and two dry or low water vapor content cases were found.

Using multi-functional lidar techniques of Doppler wind lidar and Raman lidar, the vertical wind speed and vertical water vapor flux can be obtained. Furthermore, the ascending and descending of the water vapor in a synoptic process can also be monitored.

Acknowledgements. We thanks our colleagues for their kindly support before and during the field experiment, including Kailin Zhang from Ocean University of China (OUC) for preparing the hardware and conducting the lidar transportation; Xiaochun Zhai and Dongxiang Wang for operating lidars in Naqu; Rongzhong Li and Xitao Wang from Seaglet Environment Technology for maintaining the Doppler lidar; Zhiqun Hu, Zheng Ruan and Zhehu Cui from Chinese Academy of Meteorological Science for the coordinating of field experiments; and Jianhua Ye from Genuine Optronics Limited for his kindly supplying the backup circuit of the laser. This work was partly supported by the National Natural Science Foundation of China (NSFC) under grant nos. 41375016, 41471309 and 91337103 and by the China Special Fund for Meteorological Research in the Public Interest under grant GYHY201406001. The authors gratefully acknowledge the NOAA Air Resources Laboratory (ARL) for the provision of the HYSPLIT transport and dispersion model and/or READY website (http://www.ready.noaa.gov) used in this publication.

Edited by: T. Islam

References

Ansmann, A., Wandinger, U., Riebesell, M., Weitkamp, C., and Michaelis, W.: Independent measurement of extinction and backscatter profiles in cirrus clouds by using a combined Raman elastic-backscatter lidar, Appl. Opt., 31, 7113–7131, 1992.

Behrendt, A., Wulfmeyer, V., Bauer, H.-S., Schaberl, T., Di Girolamo, P., Summa, D., Kiemle, C., Ehret, G., Whiteman, D. N., and Demoz, B. B.: Intercomparison of water vapor data measured with lidar during IHOP_2002 – Part I: Airborne to ground-based lidar systems and comparisons with chilled-mirror hygrometer radiosondes, J. Atmos. Oceanic Tech., 24, 3–21, 2007a.

Behrendt, A., Wulfmeyer, V., Schaberl, T., Bauer, H.-S., Kiemle, C., Ehret, G., Flamant, C., Kooi, S., Ismail, S., and Ferrare, R.: Intercomparison of water vapor data measured with lidar during IHOP_2002 – Part II: Airborne-to-airborne systems, J. Atmos. Oceanic Tech., 24, 22–39, 2007b.

Bhawar, R., Di Girolamo, P., Summa, D., Flamant, C., Althausen, D., Behrendt, A., Kiemle, C., Bosser, P., Cacciani, M., and Champollion, C.: The water vapour intercomparison effort in the framework of the Convective and Orographically – Precipitation Study: airborne-to-ground-based and airborne-to-airborne lidar systems, Q. J. Roy. Meteor. Soc., 137, 325–348, 2011.

Browell, E. V.: Remote sensing of tropospheric gases and aerosols with an airborne DIAL system, in: Optical and Laser Remote Sensing, Springer, Berlin Heidelberg, 138–147, 1983.

Bruneau, D., Quaglia, P., Flamant, C., Meissonnier, M., and Pelon, J.: Airborne lidar LEANDRE II for water-vapor profiling in the troposphere, I. System description, Appl. Optics, 40, 3450–3461, 2001.

Buck, A. L.: New equations for computing vapor pressure and enhancement factor, J. Appl. Meteorol., 20, 1527–1532, 1981.

Cariou, J. and Boquet, M.: LEOSPHERE Pulsed Lidar Principles, Leosphere, Orsay (France), 1–32, 2011.

Cooney, J.: Remote measurements of atmospheric water vapor profiles using the Raman component of laser backscatter, J. Appl. Meteorol., 9, 182–184, 1970.

DeFoor, T. and Robinson, E.: Stratospheric lidar profiles from Mauna Loa Observatory, winter 1985–1986, Geophys. Res. Lett., 14, 618–621, 1987.

DeFoor, T. E., Robinson, E., and Ryan, S.: Early lidar observations of the June 1991 Pinatubo eruption plume at Mauna Loa Observatory, Hawaii, Geophys. Res. Lett., 19, 187–190, 1992.

Demtröder, W.: Molecular Physics: Theoretical Principles and Experimental Methods, Wiley VCH, Weinheim, 2005.

Demtröder, W.: Laser spectroscopy: basic concepts and instrumentation, Springer Science & Business Media, Berlin Heidelberg, 2013.

Ding, Q. and Wang, B.: Circumglobal teleconnection in the northern hemisphere summer, J. Clim., 18, 3483–3505, 2005.

Dinoev, T.: Automated Raman lidar for day and night operational observation of tropospheric water vapor for meteorological applications, 2009, École Polytechnique Fédérale de Lausanne, Lausanne, 2009.

Dinoev, T., Simeonov, V., Arshinov, Y., Bobrovnikov, S., Ristori, P., Calpini, B., Parlange, M., and van den Bergh, H.: Raman Lidar for Meteorological Observations, RALMO – Part 1: Instrument description, Atmos. Meas. Tech., 6, 1329–1346, doi:10.5194/amt-6-1329-2013, 2013.

Draxler, R. R. and Rolph, G.: HYSPLIT (HYbrid Single-Particle Lagrangian Integrated Trajectory) model, NOAA Air Resources Laboratory, Silver Spring, Md, available at: http://www.arl.noaa.gov/ready/hysplit4.html (last access: 5 January 2016), 2003.

Ferrare, R., Melfi, S., Whiteman, D., Evans, K., Schmidlin, F., and Starr, D. O. C.: A comparison of water vapor measurements made by Raman lidar and radiosondes, J. Atmos. Ocean. Tech., 12, 1177–1195, 1995.

Giez, A., Ehret, G., Schwiesow, R. L., Davis, K. J., and Lenschow, D. H.: Water vapor flux measurements from ground-based vertically pointed water vapor differential absorption and Doppler lidars, J. Atmos. Oceanic Tech., 16, 237–250, 1999.

Goldsmith, J., Blair, F. H., Bisson, S. E., and Turner, D. D.: Turnkey Raman lidar for profiling atmospheric water vapor, clouds, and aerosols, Appl. Opt., 37, 4979–4990, 1998.

Grant, W. B.: Differential absorption and Raman lidar for water vapor profile measurements: a review, Opt. Eng., 30, 40–48, 1991.

He, Q., Li, C., Ma, J., Wang, H., Shi, G., Liang, Z., Luan, Q., Geng, F., and Zhou, X.: The properties and formation of cirrus clouds over the Tibetan Plateau based on summertime lidar measurements, J. Atmos. Sci., 70, 901–915, 2013.

Inaba, H.: Detection of atoms and molecules by Raman scattering and resonance fluorescence, in: Laser Monitoring of the Atmosphere, Springer, Berlin Heidelberg, 153–236, 1976.

Inaba, H. and Kobayasi, T.: Laser-Raman radar – Laser-Raman scattering methods for remote detection and analysis of atmospheric pollution, Opto-Electron., 4, 101–123, 1972.

Klanner, L., Trickl, T., and Vogelmann, H.: Combined Raman lidar and DIAL sounding of water vapour and temperature at the NDACC station Zugspitze, EGU General Assembly 2010, Vienna, Austria, 2–7 May 2010, p. 15414, 2010.

Kuwagata, T., Numaguti, A., and Endo, N.: Diurnal variation of water vapor over the central Tibetan Plateau during summer, J. Meteorol. Soc. Jpn., 2, 79, 401–418, 2001.

Larchevêque, G., Balin, I., Nessler, R., Quaglia, P., Simeonov, V., van den Bergh, H., and Calpini, B.: Development of a multiwavelength aerosol and water-vapor lidar at the Jungfraujoch Alpine Station (3580 m above sea level) in Switzerland, Appl. Opt., 41, 2781–2790, 2002.

Leblanc, T., McDermid, I. S., and Aspey, R. A.: First-year operation of a new water vapor Raman lidar at the JPL Table Mountain Facility, California, J. Atmos. Oceanic Tech., 25, 1454–1462, 2008.

Li, Y., Xu, H., and Liu, D.: Features of the extremely severe drought in the east of Southwest China and anomalies of atmospheric circulation in summer 2006, Acta Meteorol. Sin., 25, 176–187, 2011.

Liu, L., Zheng, J., Ruan, Z., Cui, Z., Hu, Z., Wu, S., Dai, G., and Wu, Y.: Comprehensive radar observations of clouds and precipitation over the Tibetan Plateau and preliminary analysis of cloud properties, J. Meteorol. Res., 29, 546–561, 2015.

Malinovskaya, S., Bucksbaum, P., and Berman, P.: Theory of selective excitation in stimulated Raman scattering, Phys. Rev. A, 69, 013801, doi:10.1103/PhysRevA.69.013801, 2004.

Melfi, S., Lawrence Jr., J., and McCormick, M.: Observation of Raman scattering by water vapor in the atmosphere, Appl. Phys. Lett., 15, 295–297, 1969.

Melfi, S.: Remote measurements of the atmosphere using Raman scattering, Appl. Opt., 11, 1605–1610, 1972.

Papayannis, A., Ancellet, G., Pelon, J., and Megie, G.: Multiwavelength lidar for ozone measurements in the troposphere and the lower stratosphere, Appl. Opt., 29, 467–476, 1990.

Park, C.-K. and Schubert, S. D.: On the nature of the 1994 East Asian summer drought, J. Clim., 10, 1056–1070, 1997.

Pelon, J. and Mégie, G.: Ozone monitoring in the troposphere and lower stratosphere: Evaluation and operation of a ground-based lidar station, J. Geophys. Res., 87, 4947–4955, 1982.

Peppler, R. A. and Lamb, P. J.: Tropospheric static stability and central North American growing season rainfall, Mon. Weather Rev., 117, 1156–1180, 1989.

Qiyun, G., Wei, L., Yucun, Z., Fengqin, L., and Peitao, Z.: Performance test and comparative analysis of GTS1, GTS1-1 and GTS1-2 radiosondes, Meteorol. Hydrol. Mar. Instrum., 1, 004, 2012.

Renaut, D. and Capitini, R.: Boundary-layer water vapor probing with a solar-blind Raman lidar: validations, meteorological observations and prospects, J. Atmos. Oceanic Tech., 5, 585–601, 1988.

Rolph, G.: Real-time Environmental Applications and Display sYstem (READY) NOAA Air Resources Laboratory, Silver Spring, Md, available at: http://www.arl.noaa.gov/ready/hysplit4.html (last access: 5 January 2016), 2003.

Sinha, A. and Harries, J. E.: Water vapour and greenhouse trapping: The role of far infra, Geophys. Res. Lett., 22, 2147–2150, 1995.

Turner, D. D. and Goldsmith J. E. M.: 24-hour Raman lidar water vapor measurements during the Atmospheric Radiation Measurement program's 1996 and 1997 water vapor intensive observation periods, J. Atmos. Oceanic Tech., 16, 1062–1076, 1999.

Vaughan, G., Wareing, D., Thomas, L., and Mitev, V.: Humidity measurements in the free troposphere using Raman backscatter, Q. J. Roy. Meteor. Soc., 114, 1471–1484, 1988.

Vogelmann, H. and Trickl, T.: Wide-range sounding of free-tropospheric water vapor with a differential-absorption lidar (DIAL) at a high-altitude station, Appl. Opt., 47, 2116-2132, 2008.

Wang, J., Carlson, D. J., Parsons, D. B., Hock, T. F., Lauritsen, D., Cole, H. L., Beierle, K., and Chamberlain, E.: Performance of operational radiosonde humidity sensors in direct comparison with a chilled mirror dew-point hygrometer and its climate implication, Geophys. Res. Lett., 30, 1860, doi:10.1029/2003GL016985, 2003.

Whiteman, D., Melfi, S., and Ferrare, R.: Raman lidar system for the measurement of water vapor and aerosols in the Earth's atmosphere, Appl. Opt., 31, 3068–3082, 1992.

Wirth, M., Fix, A., Mahnke, P., Schwarzer, H., Schrandt, F., and Ehret, G.: The airborne multi-wavelength water vapor differential absorption lidar WALES: system design and performance, Appl. Phys. B, 96, 201–213, 2009.

Wu, S., Yin, J., Liu, B., Liu, J., Li, R., Wang, X., Feng, C., Zhuang, Q., and Zhang, K.: Characterization of turbulent wake of wind turbine by coherent Doppler lidar, SPIE Newsroom, doi:10.1117/2.1201412.005658, 2014.

Wu, S., Song, X., Liu, B., Dai, G., Liu, J., Zhang, K., Qin, S., Hua, D., Gao, F., and Liu, L.: Mobile multi-wavelength polarization Raman lidar for water vapor, cloud and aerosol measurement, Opt. Express, 23, 33870–33892, 2015.

Wulfmeyer, V. and Bösenberg, J.: Ground-based differential absorption lidar for water-vapor profiling: assessment of accuracy, resolution, and meteorological applications, Appl. Opt., 37, 3825–3844, 1998.